MATERIALS SCIENCE

Wafer-scale freestanding vanadium dioxide film

He Ma[1], Xiao Xiao[1], Yu Wang[1], Yufei Sun[2], Bolun Wang[2], Xinyu Gao[3], Enze Wang[2], Kaili Jiang[3], Kai Liu[2]*, Xinping Zhang[1]*

Vanadium dioxide (VO_2), with well-known metal-to-insulator phase transition, has been used to realize intriguing smart functions in photodetectors, modulators, and actuators. Wafer-scale freestanding VO_2 (f-VO_2) films are desirable for integrating VO_2 with other materials into multifunctional devices. Unfortunately, their preparation has yet to be achieved because the wafer-scale etching needs ultralong time and damages amphoteric VO_2 whether in acid or alkaline etchants. Here, we achieved wafer-scale f-VO_2 films by a nano-pinhole permeation-etching strategy in 6 min, far less than that by side etching (thousands of minutes). The f-VO_2 films retain their pristine metal-to-insulator transition and intrinsic mechanical properties and can be conformably transferred to arbitrary substrates. Integration of f-VO_2 films into diverse large-scale smart devices, including terahertz modulators, camouflageable photoactuators, and temperature-indicating strips, shows advantages in low insertion loss, fast response, and low triggering power. These f-VO_2 films find more intriguing applications by heterogeneous integration with other functional materials.

INTRODUCTION

Smart materials have attracted remarkable academic and industrial interests in recent years with the growing interest in wearable electronics. As a well-known phase-change material, vanadium dioxide (VO_2) has been used in a lot of intriguing smart applications, including Mott transistors, strain sensors (*1*), actuators (*2*–*4*), and thermal irradiation modulators (*5*), owing to its metal-insulator phase transition (MIT) at 68°C (*6*–*9*). Integration of VO_2 with other materials not only enhances the performance of smart devices but also provides complementary functions (*10*–*14*). For example, Guo *et al.* (*10*) prepared a phase transition–tunable vertical diode based on a graphene/VO_2/BN/graphite heterostructure. The MIT of VO_2 tuned the barrier height at the VO_2/BN interface, leading to a substantial enhancement of the current density and on/off ratio. Luo *et al.* (*12*) developed a phase transition–modulated WSe_2/VO_2 photodetector, which dynamically switched from a type II heterojunction to a Schottky junction across the MIT of VO_2, resulting in both high detectivity and large responsivity in the dual working modes. Most recently, Jiang *et al.* (*14*) demonstrated that the flexoelectricity of MoS_2 can be effectively activated through the strain-gradient engineering induced by the structural phase transition of VO_2, thus achieving an ultrahigh bulk photovoltaic coefficient of MoS_2. In this regard, wafer-scale VO_2 films are highly desirable for the heterogeneous integration of multifunctional arrayed smart devices. However, the temperature required for crystallization of VO_2 phase is usually too high (>500°C) for Si-compatible processing, which may destroy other materials and induce large interface strain, thus hindering the heterogeneous integration of VO_2 with other materials.

This obstacle to heterogeneous integration can be solved by the layer-transfer method, as widely used in two-dimensional (2D) materials. In the layer-transfer method, VO_2 films are released from substrates, being freestanding VO_2 (f-VO_2) films by some etching ways, and then transferred to target substrates. Isotropic wet under-etching through a sacrificial layer is usually adopted to detach metal oxide films from substrates. However, the release time of metal-oxide films by normal under-etching ways is typically very long (*15*). For example, Shen *et al.* (*16*) reported epitaxial lift-off of $LiFe_5O_8$ film by using a $La_{0.67}Sr_{0.33}MnO_3$ sacrificial layer. Although the sample area was only 50 mm^2, the release time was longer than 24 hours. Li *et al.* (*17*) reported epitaxial lift-off of VO_2 film with an area of 900 mm^2 by using a ZnO sacrificial layer, and the release time was longer than 24 hours. Most recently, Han *et al.* (*18*) reported that ultrathin f-VO_2 films were detached from the substrate by dissolving a $Sr_3Al_2O_6$ sacrificial layer. They found that the release time could be shortened from 1440 to 10 min by inserting an Al_2O_3 buffer layer between the VO_2 layer and the $Sr_3Al_2O_6$ sacrificial layer for a sample area of 25 mm^2. However, if such an Al_2O_3-buffer-layer insertion strategy was applied to a wafer-scale sample (diameter of 2 inches), the release time would still be longer than 50 min. Moreover, Al_2O_3 under the VO_2 film blocked the contact of the VO_2 film with other materials and thus prevented the construction of VO_2 heterostructure.

The long etching time of metal oxide films from substrates leads to low fabrication efficiency, and more importantly, it may decay or even damage VO_2 films because VO_2 is amphoteric and prone to erosion of either acid or alkaline etchants (*19*). This case becomes even worse when a wafer-scale f-VO_2 film is prepared. Fast preparation of wafer-scale f-VO_2 films with minimized etching time is particularly crucial for high-performance integrated devices but unfortunately has yet to be achieved. In this work, we report a nano-pinhole permeation-etching (NPE) strategy to prepare wafer-scale f-VO_2 films in few minutes. It is realized by simultaneously etching VO_2/SiO_2 interface through the naturally formed, numerous nano-pinholes in a VO_2 film, leading to markedly reduced releasing time, far less than that for a normal dense VO_2 film by under-etching (thousands of minutes). The merits of a short release time, easy transferability, and wafer-scale sample area facilitate the application of the f-VO_2 film in various flexible integrated devices.

[1]Institute of Information Photonics Technology, Faculty of Science, Beijing University of Technology, Beijing 100124, P. R. China. [2]State Key Laboratory of New Ceramics and Fine Processing, School of Materials Science and Engineering, Tsinghua University, Beijing 100084, P. R. China. [3]State Key Laboratory of Low-Dimensional Quantum Physics, Tsinghua-Foxconn Nanotechnology Research Center, Department of Physics, Collaborative Innovation Center of Quantum Matter, Tsinghua University, Beijing 100084, P. R. China.
*Corresponding author. Email: liuk@tsinghua.edu.cn (K.L.); zhangxinping@bjut.edu.cn (X.Z.)

RESULTS

NPE strategy

A dense VO_2 film is logically preferred when preparing VO_2 thin-film devices. However, a dense film blocks wetting removal of the sacrificial layer below it, and thus only an under-etching through both sides is allowed (Fig. 1A). For a wafer-scale film, therefore, a very long releasing time is needed. In contrast, we synthesized VO_2 films with nano-pinholes on a SiO_2 substrate (SiO_2/Si or quartz substrates) via reactive magnetic sputtering and a postannealing process. With the transform of a smooth VO_x film to a granular polycrystalline VO_2 film in the postannealing process, nano-pinholes are naturally formed at the vicinity of VO_2 grain boundaries and uniformly distributed across the VO_2 film, and they allow the buffered oxide etch (BOE) solution to remove the VO_2/SiO_2 interface through NPE. The formation of the nano-pinholes is attributed to the dewetting of VO_2 film on the SiO_2 substrate in the annealing process (*20*). Because of high interfacial surface energy between VO_2 and SiO_2 at 450°C (*21*), during annealing, some voids would first nucleate at the interface and then grow toward the surface, forming nano-pinholes in the VO_2 film. The wet-etch release process occurs over the entire VO_2 film through the BOE permeation from numerous nano-pinholes, enabling the rapid one-step preparation of wafer-scale f-VO_2 films (Fig. 1B and fig. S1). As shown in Fig. 1C and fig. S1, an f-VO_2 film with an area of ~14 cm^2 was prepared by the NPE strategy and was transferred onto a polyethylene terephthalate (PET) substrate. The f-VO_2/PET film can be easily bent, demonstrating the good flexibility of the f-VO_2/PET film. Moreover, the temperature-dependent transmittance curves and Raman spectra at multiple points on the f-VO_2/PET film were measured (fig. S2A). The transmittance change amplitude, MIT temperature, and Raman spectra at these monitor points were almost the same (fig. S2, B and C), demonstrating excellent homogeneity of the f-VO_2 film in its phase-transition and structural properties. The thinnest f-VO_2 film obtained on the basis of the NPE strategy is ~20 nm (fig. S3). The releasing time via the NPE method is at least two orders of magnitude shorter than that via normal side etching (Fig. 1D).

From the scanning electron microscopy (SEM) image of an f-VO_2 film (Fig. 1E), we observed numerous nano-pinholes uniformly distributed on the f-VO_2 film, agreeing with SEM observations of the as-grown VO_2 film on the SiO_2 substrate (fig. S4). The SEM image of a cross-sectional view of an f-VO_2 film indicates that the nano-pinhole is perforated (fig. S5). From the transmission electron microscopy (TEM) image of the f-VO_2 film, we observed that the VO_2 film that detached from the SiO_2 substrate maintained a high continuity (fig. S6A), and the nano-pinholes lay at the boundaries of VO_2 crystalline grains (inset of Fig. 1E). The TEM image and the corresponding electron diffraction pattern in fig. S6 (B and C) indicate the polycrystalline structure of the f-VO_2 film. Figure S6 (D and E) shows the TEM images of nano-pinholes in f-VO_2 films with thicknesses of ~190 and ~480 nm, respectively. These nano-pinholes have the same contrast as the blank region in the TEM images, which suggests that they penetrated from the top to the bottom surface of the f-VO_2 film. The atomic structure of a VO_2 crystalline grain was also analyzed by the atomic high-angle annular dark-field scanning TEM (fig. S6F). The *d* spacing of 0.22 and 0.24 nm corresponded to the (020) plane and the (111) plane of monoclinic VO_2, respectively. The contact angle of the BOE solution on the VO_2 film is 30.3° (inset of Fig. 1F), indicating the excellent wettability of the BOE solution on the VO_2 film. According to

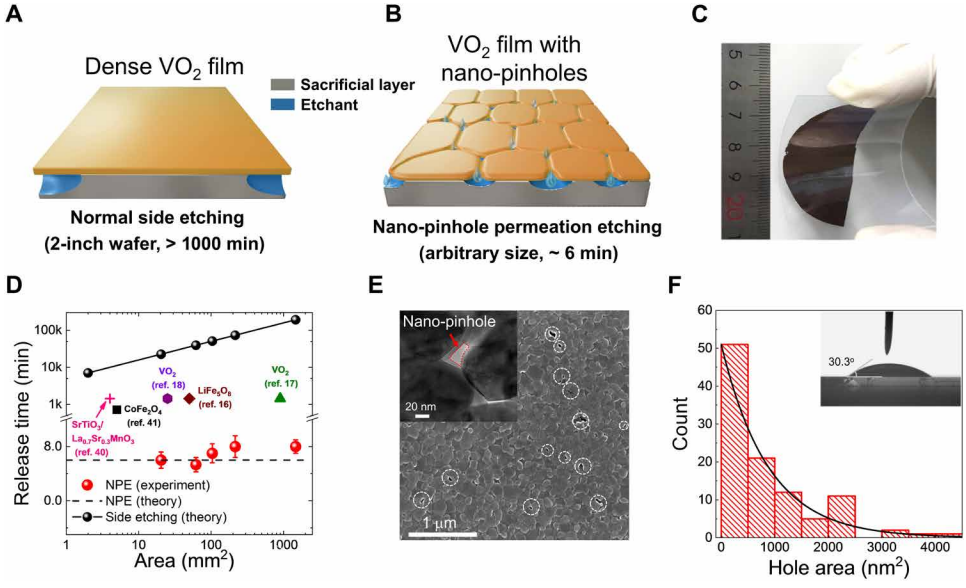

Fig. 1. NPE strategy for preparation of the large-area f-VO_2 film. (**A**) Schematic diagram of the normal side-etching method. (**B**) Schematic diagram of the NPE strategy. (**C**) Optical image of f-VO_2 film transferred to a polyethylene terephthalate substrate. Photo credit: He Ma, Beijing University of Technology. (**D**) Comparison of the release time by the NPE and the normal side-etching method. The cross, square, hexagon, diamond, and triangle correspond to the release time of $SrTiO_3$/$La_{0.7}Sr_{0.3}MnO_3$ film (*40*), $CoFe_2O_4$ film (*41*), VO_2 film (*18*), $LiFe_5O_8$ film (*16*), and VO_2 film (*17*) by the normal side-etching method, respectively. The theoretical release time required by the normal side-etching method was calculated by the model in fig. S7D. (**E**) Scanning electron microscopy (SEM) and transmission electron microscopy images of an f-VO_2 film. The nano-pinholes are marked by circles. (**F**) Histogram of the area of nano-pinholes on the VO_2 film. The inset shows the contact angle of the BOE solution on the as-grown VO_2 film.

Zisman's equation, a low–surface energy liquid wets out a higher–surface energy solid surface. Therefore, the nano-pinholes with high surface energy enhance the wettability of the etchant on the VO_2 film. Moreover, the capillary force also facilitates the etchant to enter the hydrophilic nano-pinholes. Therefore, the nano-pinholes in the VO_2 film work as permeation paths for the etchant to remove the SiO_2 sacrificial layer. Figure 1F and fig. S7A show statistics from multiple SEM images of the f-VO_2 film, indicating that most of the nano-pinholes have an area of 500 nm^2 and that the average number of nano-pinholes in an f-VO_2 film is eight pinholes per 10 μm^2. On the basis of these statistics, we built a model for the wet-etch release of the VO_2 film (fig. S7B). For a nano-pinhole with an area of 500 nm^2, the BOE solution should etch the SiO_2 sacrificial layer over an area of 1.12 μm by 1.12 μm and release the VO_2 film. The typical etching rate of the BOE solution (5:1 volume ratio of 40% NH_4F to 49% HF) is 100 nm/min (*22*). Hence, the theoretical release time for the VO_2 film is 6 min, which is in agreement with our experimentally determined value (average, 6.8 min; Fig. 1D). In addition, the release time for f-VO_2 films with different areas is almost the same, indicating a simultaneous etching of the interface layer in the whole VO_2 film. According to the geometrical model in fig. S7C, assuming that the nano-pinholes are cylinder-shaped with the mean diameter of 25 nm and a pitch of 1.12 μm, a 200-nm-thick VO_2 film with the nano-pinholes only increase by ~1.3% in the contact surface area compared with a dense VO_2 film. Such a small increase in the surface area will not make the VO_2 film erode more easily.

Phase-transition, structural, and mechanical properties of f-VO_2 films

We studied the property of the f-VO_2 film in three aspects: first, the phase transition of the f-VO_2 film in its optical and electrical properties; second, the structural property of the f-VO_2 film; and third, the mechanical property of the f-VO_2 film. To reveal the intrinsic phase-transition property of the f-VO_2 film, we suspended f-VO_2 films with different thicknesses on holes and measured the temperature-dependent transmission curves. As shown in fig. S8, the transmittance of the 90-nm-thick f-VO_2 film at the wavelength of 1600 nm drastically decreases as the temperature increases from 25° to 90°C, indicating that there is a phase transition in the f-VO_2 film. We also transferred the 190-nm-thick f-VO_2 film to a carbon nanotube (CNT) film with a 6-mm-diameter hole (Fig. 2A), and the area of the resulting suspended VO_2 film reached 28 mm^2. Under current heating, the transmittance of the f-VO_2 film decreases from 49.5 to 0.8% as the power density increases to 6.7 mW/mm^2 (Fig. 2B). Although the suspended VO_2 film is not heated directly, the Joule heat generated from the CNT film transfers to the suspended VO_2 film and causes a phase transition.The optical modulation amplitude of the f-VO_2 films is comparable with epitaxial VO_2 films and other VO_2 films supported by substrates in the literature (table S1), suggesting that our f-VO_2 films with nano-pinholes have high quality in the optical property. The resistance-temperature curve of an f-VO_2 film suspended on a $Si_3N_4/SiO_2/Si$ frame is shown in Fig. 2C and compared with an as-grown VO_2 film. The f-VO_2 film and the as-grown VO_2 film present resistance change ratios from 30° to 90°C of more than three orders of magnitude. The higher resistance change ratio of our f-VO_2 films than other freestanding VO_2 membranes (table S2) indicates the high quality of our films in the electrical transport property. In addition, the f-VO_2 film has a slightly wider hysteresis than the as-grown VO_2 film. This phenomenon can be ascribed to the strain effect. Chen *et al.* (*23*) studied the influence of the strain on the thermal hysteresis of the VO_2/muscovite film. They found that the thermal hysteresis would be wide

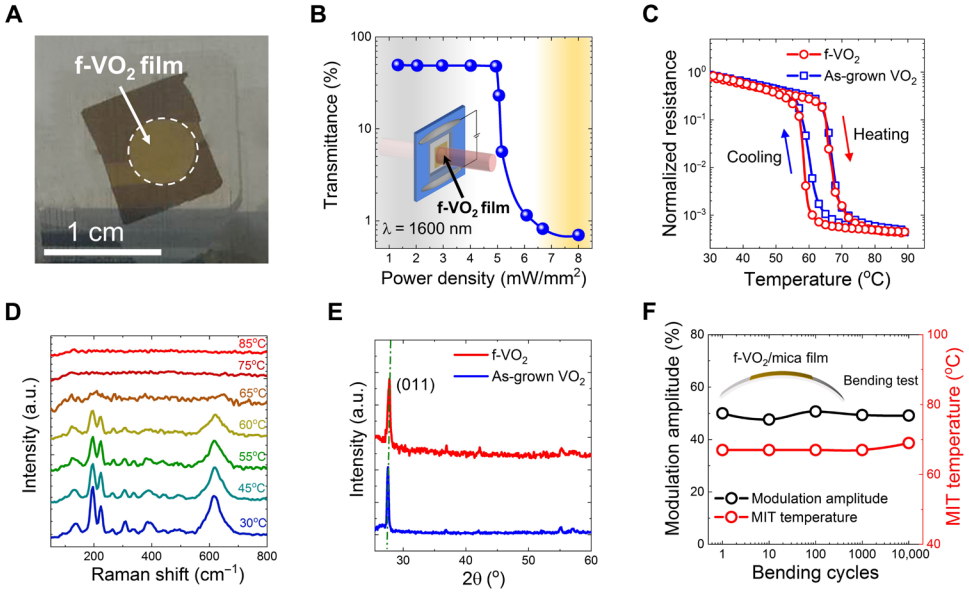

Fig. 2. Phase-transition, structural, and mechanical properties of the f-VO_2 film. (**A**) Optical image of the f-VO_2 film suspended on a CNT film with a hole at its center. Photo credit: He Ma, Beijing University of Technology. (**B**) Change of the transmittance of the 190-nm-thick f-VO_2 film at the wavelength of 1600 nm with power density. Inset is the schematic diagram for measuring the change of transmittance of the f-VO_2 film under electrical stimulation. (**C**) Resistance-temperature curves for the f-VO_2 film suspended on a silicon-nitride frame and the as-grown VO_2 film. (**D**) Change of the Raman spectrum of the f-VO_2 film transferred to the quartz substrate with temperature. a.u., arbitrary units. (**E**) XRD spectra for the as-grown VO_2 film and the f-VO_2 film suspended on the quartz frame. (**F**) Modulation amplitude and MIT temperature of the f-VO_2/mica film as a function of bending cycles under the curvature of 240 m^{-1}.

under a compressive strain and be narrow under a tensile strain. Therefore, if an as-grown VO_2 film suffers from a tensile strain induced by a substrate, then the released f-VO_2 film has a wider thermal hysteresis due to the strain relaxation. Large area–suspended VO_2 film, being free from the confinement of the substrate, provides a high degree of freedom for tuning the property of VO_2 such as applying stress and facilitates the construction of smart devices with high sensitivity to environmental changes.

To reveal the structural property of the f-VO_2 film, we studied morphology, Raman spectrum, and x-ray diffraction (XRD) of the f-VO_2 film and compared them with the as-grown VO_2 film. The surface morphology of the f-VO_2 film transferred to a quartz substrate is almost the same as that of the as-grown VO_2 film (fig. S9). Figure 2D and fig. S10 show the Raman spectra of the f-VO_2 film transferred to the quartz substrate, confirming that the f-VO_2 film is in the M1 insulating phase (*24*). With increasing temperature, the intensity of the Raman peaks gradually decreases and then disappears when the temperature is >65°C, which demonstrates the phase transition of the f-VO_2 film (Fig. 2D). The XRD spectrum indicates that the f-VO_2 film is textured along the (110) plane of the M1 insulating phase (Fig. 2E). The XRD spectrum of the f-VO_2 film is nearly identical to the as-grown VO_2 film, indicating that the f-VO_2 film has excellent structural stability during the release and transfer processes.

The mechanical properties of the f-VO_2 film were studied using a micromanipulator mounted in a scanning electron microscope (fig. S11A). As shown in fig. S11 (B and C), the 120-nm-thick f-VO_2 nanobelt can reach a maximum bending curvature of up to 0.184 μm^{-1}, and the nanobelt fractures on further bending (fig. S11D). Hence, the maximum bending strain of the f-VO_2 nanobelt is determined to be 1.2%, which is larger than that of the bulk of VO_2 crystal (<1%) (*25*). We also studied the influence of the nano-pinholes on the mechanical deformation of the VO_2 film by the finite element method. A 0.1-μN force is applied on one end of VO_2 films. As shown in fig. S12, the curvature of the VO_2 film with nano-pinholes is the same as that of the dense VO_2 film, demonstrating that the existence of nano-pinholes does not affect the mechanical deformation of the VO_2 film. Last, a 190-nm-thick f-VO_2 film was transferred to a flexible mica substrate (fig. S13, A to C), and a bending test was performed to test the durability of the f-VO_2/mica film. The transmittance-temperature curve of the f-VO_2/mica film (fig. S13D) was measured after bending over 1, 10, 100, 1000, and 10,000 cycles under the curvature of 240 m^{-1}. The modulation amplitude and the MIT temperature were used to evaluate the phase-transition properties of the f-VO_2/mica film. As shown in Fig. 2F, both the modulation amplitude and the MIT temperature are not altered with bending. Because a robust electrical MIT of a VO_2 film is essential in flexible VO_2 electrical devices, we also measured the electrical property of the f-VO_2/mica film as a function of the curvature and bending cycles. As shown in fig. S14 (A and B), the electrical conductivity, the resistance change ratio from 30° to 90°C, and the MIT temperature of the VO_2/mica film are not altered with the curvature and bending cycles. The above bending tests demonstrate excellent mechanical stability of the f-VO_2/mica film.

The f-VO_2 film distinguishes and surpasses typical VO_2 films on substrates in several aspects. First, the f-VO_2 film has an ultralow thermal capacity and high transparency in the terahertz (THz) range. To demonstrate this, we prepared THz modulators using f-VO_2 films. The insertion loss, the response speed, and the triggering power of these THz modulators were greatly improved. Second, f-VO_2 films can be stuck on arbitrary substrates, and diverse heterogeneous devices can be easily constructed. To demonstrate this, we fabricated a camouflageable photoactuator based on a bimorph structure composed of the f-VO_2 film and the butterfly wing. The f-VO_2/butterfly wing actuator has an ultralow triggering power (42 mW/cm^2), much lower than the solar constant (136 mW/cm^2). Moreover, f-VO_2–covered butterfly wing shows camouflageable ability in the visible and infrared (IR) spectral regions. In addition, we used the f-VO_2/polyimide (PI) film as a flexible temperature-indicating strip (TIS) to monitor thermodiffusion, and the IR imaging contrast of the region where VO_2 TIS attached was substantially enhanced.

THz modulator based on f-VO_2 films

The considerable modulation depth, low insertion loss, broadband response, and multistimulation enable VO_2 to be an ideal THz modulation material (*26*, *27*). However, the development of VO_2-based THz modulators with high performance is still a great challenge. The substrate is one of the factors that limit the performance of VO_2-based THz modulators. First, absorption of THz radiation by the substrate increases the insertion loss. Second, the substrate's large thermal capacity increases the triggering threshold and the response time of VO_2-based THz modulators. Therefore, a THz modulator based on f-VO_2 films is of marked interest because the freestanding nature of the film effectively avoids the negative influence of the substrate and thus enhances the performance of the VO_2-based THz modulator.

For preparing an electrically triggered VO_2-based THz modulator, we transferred f-VO_2 films to CNT films (Fig. 3A). The optical microscopy image of the f-VO_2/CNT film is shown in fig. S15. The cross-stacked CNT film on the surface of the VO_2 film forms an ultrathin conductive network, which enables fast electrical modulation of the f-VO_2 film. We studied the spectral changes of f-VO_2/CNT films under electrical stimulation by the THz time-domain spectroscopy. As shown in Fig. 3B, for the 190-nm-thick f-VO_2 film, the average transmittance of the f-VO_2/CNT film attains 0.92 in the THz range from 0.2 to 2 THz, meaning an ultralow insertion loss of 0.36 dB. The maximum modulation depth of the f-VO_2/CNT film attains 84% under electrical stimulation with a power density of 7.5 mW/mm^2. This high modulation depth exceeds the values of many of VO_2 films with similar thicknesses and reaches the level of epitaxial VO_2 films (table S3). The triggering electrical power of typical VO_2 THz modulators fabricated on substrates ranges from 14 to 3000 mW/mm^2 (*28*–*30*). The f-VO_2/CNT film's triggering power is lower than these devices, which is attributed to the small thermal capacity of the f-VO_2/CNT film. With increasing VO_2 thickness to ~480 nm, the maximum modulation depth further increases to 94% (fig. S16). In Fig. 3C, we compared the modulation performance of the f-VO_2/CNT film (modulation depth versus insertion loss) with other types of THz modulators. Because of its high intrinsic transparency to THz wave and no absorption of substrates, the THz modulator based on f-VO_2 film presents the lowest insertion loss. Although the modulation depth of the f-VO_2 film seems to be lower than some 2D materials and VO_2 metasurface, it can be increased by further increasing the thickness of the f-VO_2 film. Moreover, optical modulators with an extinction ratio larger than 7 dB (modulation depth > 0.8) are preferable for most applications (*31*). Therefore, the modulation depth

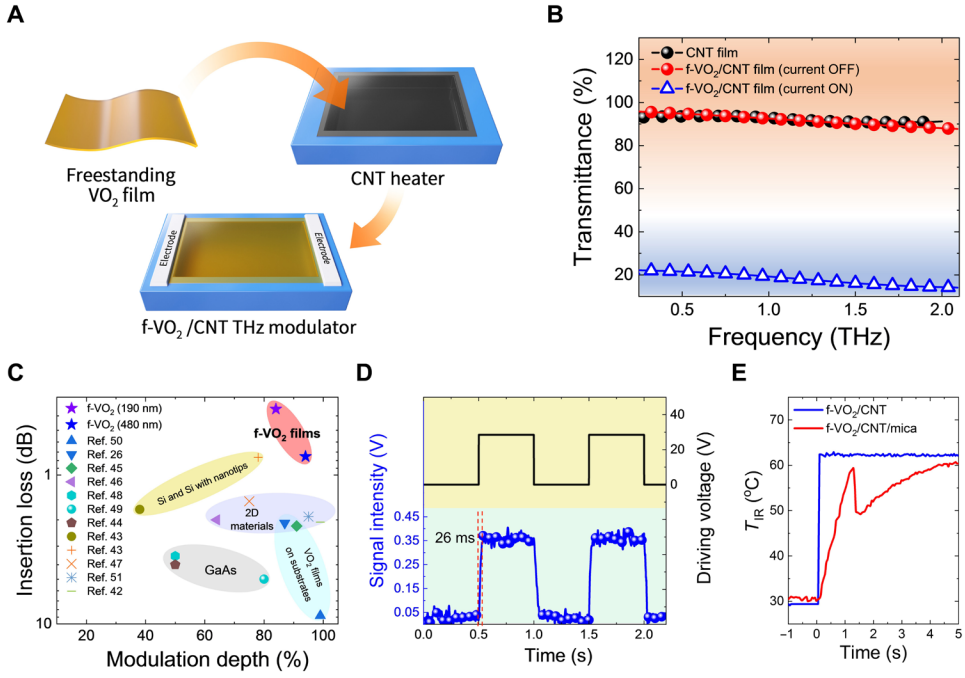

Fig. 3. THz modulator based on the f-VO_2/CNT film. (**A**) Schematic diagram for preparing a THz modulator by sticking the f-VO_2 film on a CNT film. (**B**) Transmittance of the CNT film, the f-VO_2/CNT film, and the f-VO_2/CNT film under electrical stimulation with a power density of 7.5 mW/mm^2 in the frequency range from 0.2 to 2 THz. (**C**) Comparison of the insertion loss and the modulation depth of the f-VO_2/CNT THz modulator with other current-triggered or light-triggered THz modulators on substrates (*26*, *42*–*51*). (**D**) Transient response of the suspended f-VO_2/CNT film under a square wave–modulated voltage with a frequency of 1 Hz. (**E**) Nominal thermographic temperature (T_{IR}) changes of the f-VO_2/CNT film and the f-VO_2/CNT/mica film under electrical stimulation.

of our f-VO_2/CNT film is enough to satisfy the engineering requirement. Figure 3D and fig. S17 show the transient response of the f-VO_2/CNT film under a square wave–modulated voltage with a frequency of 1 Hz, indicating that the typical response time of our f-VO_2/CNT film is only 26 ms. The response time of the f-VO_2/CNT film is almost one order of magnitude shorter than other THz modulators based on VO_2 film grown on substrates (*28*, *32*). To further study the influence of the thermal capacity on the device performance, the nominal thermographic temperature (T_{IR}) changes of the f-VO_2/CNT film and a VO_2/CNT/mica film under the electrical stimulation were measured by the thermographic camera (fig. S18). As shown in Fig. 3E, the response time of the f-VO_2/CNT film is less than 50 ms (equipment response limit), far less than that of the f-VO_2/CNT/mica film (5 s). These results suggest that the ultralow thermal capacity of the f-VO_2/CNT film effectively shortens the response time. Therefore, the considerable modulation depth, low insertion loss, low triggering power, and fast response of the f-VO_2/CNT film allow it to function as an excellent active THz modulator.

Camouflageable photoactuator

The freestanding nature of the f-VO_2 film allows it to be conformally attached to any substrate. In addition to common flexible substrates such as PI and PET films, the f-VO_2 film can also be stuck on biological organisms to construct functional devices. A flexible actuator is a device that converts external stimulus to a mechanical motion. The inspiration of flexible actuators usually comes from an imitation of animals and plants. For many animals and plants, active color change can help them to hunt or escape. Therefore, flexible actuators with a color change function recently attracted much attention because of their potential in the application of camouflageable bionic robots (*33*–*35*). However, until now, it is still a great challenge to construct a flexible actuator with a color change function by a simple method. Here, we stuck the f-VO_2 film on a blue-morpho butterfly wing to build a camouflageable photoactuator (Fig. 4A). Under external stimulation, the photoactuator can deliver a bending motion and change its color and IR irradiation.

The morphology of the bimorph comprising the VO_2 film and the butterfly wing is shown in the lower panel of Fig. 4A, which demonstrates that the f-VO_2 film fully covers the scales of the butterfly wing. The structure color of the butterfly wing is not shielded by the VO_2 film, but strongly modified because of the environmental medium change induced by the covering of the VO_2 layer (Fig. 4B and fig. S19A). Two basic optical processes exist in the VO_2-covered butterfly wing (fig. S19B): (1) interference between light reflection/scattering at the lamella interfaces and (2) the grating diffraction by the tree-like structures. The blue color of the butterfly wing originates mainly from the interference effect by the lamella structures. Meanwhile, the diffraction of light by the large-scale tree-like structures with roughly periodic arrangements modifies further the structural colors. However, effect (2) is much weaker than (1) because of the weaker periodicity. Apparently, for both cases, a VO_2 film covering the wing surface changes the environmental refractive index of lamellae and tree-like structures. The MIT of VO_2, which leads to a large change of the refractive index, tunes the structure colors of the butterfly wing and makes the observed colors more abundant (Fig. 4B and fig. S19A). These changes of structure color are further verified by the reflection spectra from the VO_2-covered

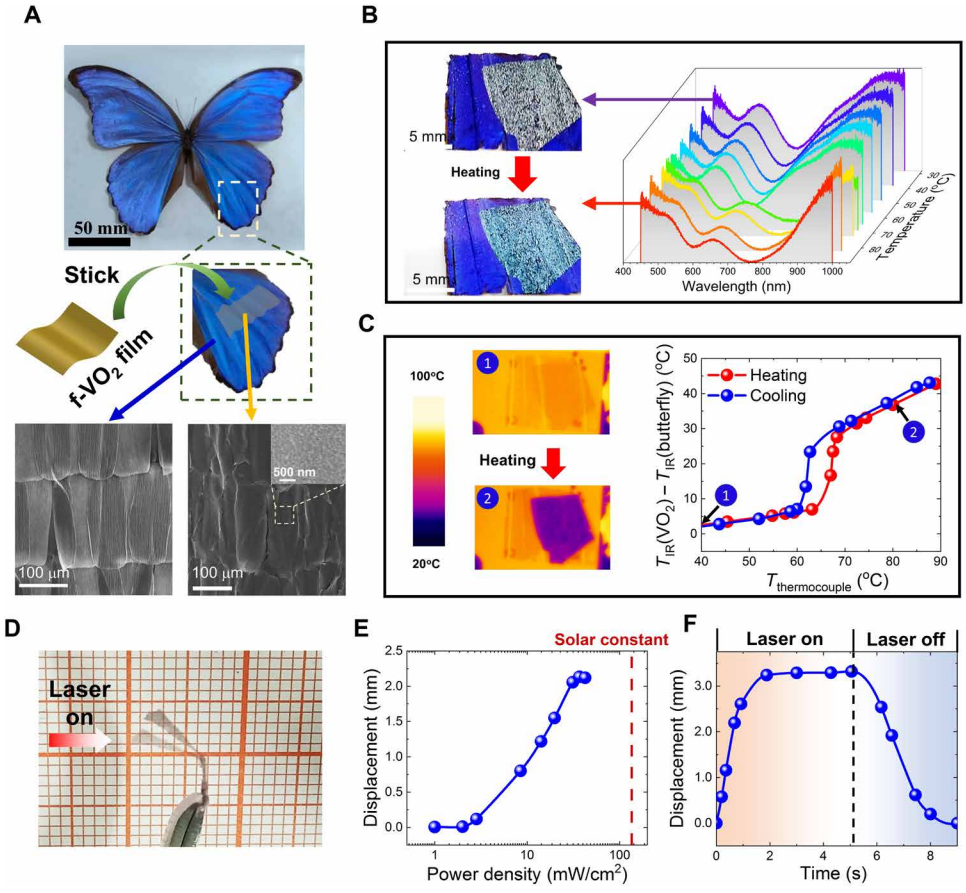

Fig. 4. Camouflageable photoactuator prepared by combining an f-VO_2 film and the butterfly wing. (**A**) Optical image of a blue-morpho butterfly specimen and schematic diagram for sticking the f-VO_2 film on the wing of the blue-morpho butterfly. SEM images at the lower panel show morphology of scales in the butterfly wing, VO_2-covered scales, and an enlarged view of the VO_2 film on the scales. The thickness of the VO_2 film was 280 nm. Photo credit: He Ma, Beijing University of Technology. (**B**) Thermochromism of the VO_2-covered butterfly wing in the wavelength range of 0.4 to 1 μm and change of the reflection spectrum with temperature. (**C**) IR images of the VO_2-covered butterfly wing at 40° and 80°C and comparison of VO_2-covered butterfly wing's temperature measured by a thermographic camera and measured by a thermocouple. (**D**) Movement of a VO_2-covered butterfly wing under light stimulation (42 mW/cm^2). (**E**) Tip displacement of the VO_2-covered butterfly wing versus power density of light. (**F**) Transient response of the VO_2-covered butterfly wing under light stimulation.

butterfly wing. As shown in the right panel of Fig. 4B, at 30°C, two spectral valleys are observed at 523 and 686 nm, respectively. Because of the MIT of VO_2, these two spectral valleys shift to 602 and 769 nm, respectively, when the temperature increases to be >68°C.

VO_2-covered butterfly wing also changes its IR irradiation in the mid-IR wavelength range more than 8 to 14 μm (Fig. 4C), which can be observed using a thermographic camera. The thermographic camera's emissivity was set to be 0.95, and the actual temperature of the butterfly wing was monitored via the neighboring thermocouple. When the temperature is higher than 68°C, the color of the thermogram of the VO_2-covered butterfly wing varies from yellow to purple, indicating that the thermographic temperature of the wing is lower than the surrounding environment. We extracted the temperature at the monitoring point on the butterfly wing ($T_{butterfly}$) from the thermogram and compared it with the thermocouple's temperature ($T_{thermocouple}$). In the temperature ($T_{thermocouple}$) range from 25° to 63°C, the temperature difference between $T_{butterfly}$ and $T_{thermocouple}$ is less than 7°C, and there is an abrupt increase to 27.6°C when the $T_{thermocouple}$ is at 68.3°C. The reflectance of M-phase VO_2 is higher than that of the I-phase VO_2 in the mid-IR region and thus absorbed fewer IR photons (*36*). According to Kirchhoff's law of radiation, the thermal radiation of the M-phase VO_2 decreases because of lower IR absorption. Therefore, when the VO_2 undergoes a phase transition, the VO_2-covered butterfly wing appears colder than the surroundings.

As shown in Fig. 4D, photothermally stimulated structural change of the VO_2 layer on the butterfly wing can drive bending of the VO_2-covered butterfly wing. The laser irradiation power required to trigger the motion of the VO_2-covered butterfly wing ranges from 3 to 42 mW/cm^2 (Fig. 4E). The ultralow triggering power can be attributed to the butterfly wing's low thermal conductivity. Figure 4F shows the transient response of the VO_2-covered butterfly wing. The rising time is 1.88 s and the recovery time is 3.95 s. The butterfly wing's low thermal conductivity results in a long recovery time. The successful construction of the camouflageable photoactuator based on the bimorph of the f-VO_2 film and the butterfly wing demonstrates that the f-VO_2 film can adapt to organic substrates with complex morphologies. The finding provides a strategy to develop high-performance macroscopic mechanical devices.

Flexible VO_2 TIS

Monitoring thermodiffusion caused by a temperature gradient is of importance in many fields such as industrial monitoring and control and solar energy performance monitoring. When observing through a thermographic camera, the most notable temperature gradient in the visual field always dominates the thermogram, resulting in an area with a small temperature gradient that is difficult to observe in real time. The thermographic camera senses the IR irradiation of the object at specific wavelengths and displays the temperature according to the equation $P = \varepsilon \cdot \sigma \cdot T^4$, where P is the radiated power, ε is the emissivity, and σ is the Stefan-Boltzmann constant. In the measurement, the thermographic camera assumes a constant wavelength-integrated emissivity for the object. Because the MIT-induced emissivity decreases, T_{IR} of the metal-phase VO_2 film greatly decreases, but T_{IR} of the other regions does not change, leading to the formation of a large nominal temperature different in the thermographic camera. These VO_2 properties allow the use of flexible VO_2 films as TISs to enhance thermographic contrast (fig. S20A). A flexible VO_2 TIS was fabricated via transfer of a large-area f-VO_2 film onto a PI film, followed by cutting to a rectangular shape. The flexible VO_2 TIS was attached to a pillar (fig. S20B). A heating pad heated one end of the pillar, and thus a temperature gradient formed along the pillar. We performed a transient temperature measurement to the pillar with the thermographic camera. Because the VO_2 TIS is very thin (300 nm/100 μm), its thermal capacitance is negligible. Therefore, the temperature profile of the VO_2/PI film is almost determined by the underneath pillar (fig. S21). Thermograms of the pillar with the VO_2 TIS at different temperatures are shown in fig. S20C. We set a temperature monitor on the thermogram, which was marked by the black cross. The temperatures at the black cross are 70°, 75°, and 80°C, which correspond with the upper, middle, and lower panels, respectively. In the thermogram, the color of the f-VO_2/PI film changes from orange to dark purple on passing the MIT of VO_2. As the temperature increases, the area of the M-phase VO_2 increases along the pillar, indicating the direction of the thermal flux. However, in the thermograms without the VO_2 TIS, the thermal flux is barely observable. As shown in fig. S20D, the maximum temperature difference along the "A" dashed line is 41°C, much larger than that along the "B" dashed line (8.2°C). Therefore, in the thermogram, the contrast of the region where the VO_2 TIS attaches is enhanced, facilitating observation of this site of interest with a small temperature gradient. If the emissivity of the M-phase VO_2 TIS is corrected in advance, then the nominal temperature difference along the A dashed line can be recovered to the actual temperature difference by adjusting the emissivity in the thermographic camera. The applicative temperature range of the VO_2 TIS is near its MIT temperature. Because the MIT temperature of VO_2 can be conveniently tuned from 72° to −100°C by elemental doping (*37*, *38*), VO_2 TIS with different applicative temperatures would be developed by using element-doped f-VO_2 films and thus finds applications in more fields such as biomedical, food safety, electronics, and so on.

DISCUSSION

In summary, we developed an NPE method for fast preparing large-area f-VO_2 films. By uniformly distributed nano-pinholes in the VO_2 film as pathways for the etchant, VO_2/SiO_2 interface can be quickly removed, and f-VO_2 films can be obtained. The area of the f-VO_2 film attained ~14 cm^2, whereas its release time was only 6 min. The advantages of a short release time, easy transferability, wafer-scale sample area, excellent phase-transition property, and ultralow thermal capacity facilitate the use of the f-VO_2 films for diverse flexible-device applications. To demonstrate the superiority of the f-VO_2 film, we coupled the f-VO_2 films with a CNT film, a butterfly wing, and a PI film to construct an active THz modulator, a camouflage photoactuator, and a flexible TIS, respectively. Further applications of the f-VO_2 film can be expected in the future via coupling f-VO_2 films with other functional materials.

MATERIALS AND METHODS

Synthesis of the VO_2 film with nano-pinholes on SiO_2 substrate

VO_x was deposited onto SiO_2/Si substrates or quartz substrates using a reactive magnetron sputtering system and a high-purity vanadium metal target. Sputtering was performed using flowing gas mixtures [typically, 30 standard cm^3/min (sccm) of Ar and 20 sccm of 96% Ar/4% O_2] at 0.6 Pa and a DC power of 55 W at 25°C. After VO_x deposition, the VO_x film was annealed in a low-pressure oxygen atmosphere (4.5 Pa) at 450°C for 10 min so that it could crystallize into a VO_2 film with nano-pinholes.

Device preparations

For preparing the THz modulator based on f-VO_2/CNT film, CNT films were drawn from a super-aligned CNT array (*39*) and cross-stacked on a quartz frame. Then, the cross-stacked CNT film was treated with oxygen plasma to enhance its hydrophilicity. Subsequently, an f-VO_2 film was released from a substrate by the NPE method and was transferred to float on clean water and finally scooped by the cross-stacked CNT film. For preparing the VO_2-covered butterfly wing, a small piece of butterfly wing was cut by scissors. Next, the butterfly wing was treated with oxygen plasma to enhance its hydrophilicity. After that, the f-VO_2 film was released from the substrate by the NPE method and was transferred to float on clean water, and last, the f-VO_2 film was scooped by the butterfly wing. For preparing the VO_2 TIS, the f-VO_2 film was released from the substrate by the NPE method and was transferred to float on clean water. Then, the f-VO_2 film was scooped by a PI film, and last, we cut the VO_2/PI film to the desired size.

Characterizations

SEM imaging was performed by a scanning electron microscope (FEI Nova NanoSEM 450). TEM imaging was performed by transmission electron microscopes (FEI Tecnai G2 F30 and FEI Titan 80-300). Atomic force microscopy imaging was performed by an atomic force microscope (WITec alpha 300). Raman spectra measurements were performed using a Jobin Yvon LabRAM HR800. The contact angle of the BOE solution on the VO_2 film was measured by a contact angle meter (Shanghai Fangrui Instrument Co., Ltd.). XRD measurements were performed using a Rigaku x-ray diffractometer. The electrical property of the VO_2 film was measured using a cascade probe station with an Agilent B2900 source meter. The optical property of the VO_2 film was measured by a Hitachi U4100 ultraviolet/visible/near-IR spectrometer. The optical property of the VO_2 film suspended on the copper grid was measured by a homemade microscope spectrophotometer coupled with an optical fiber spectrometer (Ocean Optics, NIRQuest). Sample temperatures

were controlled using a homemade hot plate, whose temperature could be tuned precisely from 20° to 100°C by a temperature controller (Model 335, Lake Shore Cryotronics Inc.). The mechanical property of the VO_2 film was measured by a micromanipulator (Kleindiek MM3A-EM) mounted in the scanning electron microscope. Thermograms were recorded by a thermographic camera (Optris PI650). A THz time-domain spectrometer (THz-TDS, Daheng Co. Ltd.) was used to measure the THz modulation property of the f-VO_2/CNT film. For measuring the transient response of the f-VO_2/CNT film, the time-delay line of the THz-TDS system was stopped at the position of the maximum THz transmission amplitude. A square wave–modulated voltage with a frequency of 1 Hz was used to trigger the f-VO_2/CNT film. The dynamical response of the THz transmission amplitude was obtained from the analogy output of the lock-in amplifier and recorded by an oscilloscope.

SUPPLEMENTARY MATERIALS

Supplementary material for this article is available at https://science.org/doi/10.1126/sciadv.abk3438

REFERENCES AND NOTES

1. B. Hu, Y. Ding, W. Chen, D. Kulkarni, Y. Shen, V. V. Tsukruk, Z. L. Wang, External-strain induced insulating phase transition in VO_2 nanobeam and its application as flexible strain sensor. *Adv. Mater.* **22**, 5134–5139 (2010).
2. H. Ma, J. Hou, X. Wang, J. Zhang, Z. Yuan, L. Xiao, Y. Wei, S. Fan, K. Jiang, K. Liu, Flexible, all-inorganic actuators based on vanadium dioxide and carbon nanotube bimorphs. *Nano Lett.* **17**, 421–428 (2017).
3. K. Liu, C. Cheng, J. Suh, R. Tang-Kong, D. Fu, S. Lee, J. Zhou, L. O. Chua, J. Wu, Powerful, multifunctional torsional micromuscles activated by phase transition. *Adv. Mater.* **26**, 1746–1750 (2014).
4. K. Liu, C. Cheng, Z. Cheng, K. Wang, R. Ramesh, J. Wu, Giant-amplitude, high-work density microactuators with phase transition activated nanolayer bimorphs. *Nano Lett.* **12**, 6302–6308 (2012).
5. L. Xiao, H. Ma, J. Liu, W. Zhao, Y. Jia, Q. Zhao, K. Liu, Y. Wu, Y. Wei, S. Fan, K. Jiang, Fast adaptive thermal camouflage based on flexible VO_2/Graphene/CNT thin films. *Nano Lett.* **15**, 8365–8370 (2015).
6. K. Liu, S. Lee, S. Yang, O. Delaire, J. Wu, Recent progresses on physics and applications of vanadium dioxide. *Mater. Today* **21**, 875–896 (2018).
7. S. Lee, K. Hippalgaonkar, F. Yang, J. Hong, C. Ko, J. Suh, K. Liu, K. Wang, J. J. Urban, X. Zhang, C. Dames, S. A. Hartnoll, O. Delaire, J. Wu, Anomalously low electronic thermal conductivity in metallic vanadium dioxide. *Science* **355**, 371–374 (2017).
8. Y. Ke, S. Wang, G. Liu, M. Li, T. J. White, Y. Long, Vanadium dioxide: The multistimuli responsive material and its applications. *Small* **14**, 1802025 (2018).
9. H. Ma, X. Xiao, X. Zhang, K. Liu, Recent advances for phase-transition materials for actuators. *J. Appl. Phys.* **128**, 101101 (2020).
10. Y. Guo, X. Sun, J. Jiang, B. Wang, X. Chen, X. Yin, W. Qi, L. Gao, L. Zhang, Z. Lu, R. Jia, S. Pendse, Y. Hu, Z. Chen, E. Wertz, D. Gall, J. Feng, T. M. Lu, J. Shi, A reconfigurable remotely epitaxial VO_2 electrical heterostructure. *Nano Lett.* **20**, 33–42 (2020).
11. W. Jiang, T. Zheng, B. Wu, H. Jiao, X. Wang, Y. Chen, X. Zhang, M. Peng, H. Wang, T. Lin, H. Shen, J. Ge, W. Hu, X. Xu, X. Meng, J. Chu, J. Wang, A versatile photodetector assisted by photovoltaic and bolometric effects. *Light Sci. Appl.* **9**, 160 (2020).
12. H. Luo, B. Wang, E. Wang, X. Wang, Y. Sun, Q. Li, S. Fan, C. Cheng, K. Liu, Phase-transition modulated, high-performance dual-mode photodetectors based on WSe_2/VO_2 heterojunctions. *Appl. Phys. Rev.* **6**, 041407 (2019).
13. B. Wang, R. Peng, X. Wang, Y. Yang, E. Wang, Z. Xin, Y. Sun, C. Li, Y. Wu, J. Wei, J. Sun, K. Liu, Ultrafast, kinetically limited, ambient synthesis of vanadium dioxides through laser direct writing on ultrathin chalcogenide matrix. *ACS Nano* **15**, 10502–10513 (2021).
14. J. Jiang, Z. Chen, Y. Hu, Y. Xiang, L. Zhang, Y. Wang, G. C. Wang, J. Shi, Flexo-photovoltaic effect in MoS_2. *Nat. Nanotechnol.* **16**, 894–901 (2021).
15. H. S. Kum, H. Lee, S. Kim, S. Lindemann, W. Kong, K. Qiao, P. Chen, J. Irwin, J. H. Lee, S. Xie, S. Subramanian, J. Shim, S. H. Bae, C. Choi, L. Ranno, S. Seo, S. Lee, J. Bauer, H. Li, K. Lee, J. A. Robinson, C. A. Ross, D. G. Schlom, M. S. Rzchowski, C. B. Eom, J. Kim, Heterogeneous integration of single-crystalline complex-oxide membranes. *Nature* **578**, 75–81 (2020).
16. L. Shen, L. Wu, Q. Sheng, C. Ma, Y. Zhang, L. Lu, J. Ma, J. Ma, J. Bian, Y. Yang, A. Chen, X. Lu, M. Liu, H. Wang, C. L. Jia, Epitaxial lift-off of centimeter-scaled spinel ferrite oxide thin films for flexible electronics. *Adv. Mater.* **29**, 1702411 (2017).
17. X. Li, Z. Yin, X. Zhang, Y. Wang, D. Wang, M. Gao, J. Meng, J. Wu, J. You, Epitaxial liftoff of wafer-scale VO_2 nanomembranes for flexible, ultrasensitive tactile sensors. *Adv. Mater. Technol.* **4**, 1800695 (2019).
18. K. Han, L. Wu, Y. Cao, H. Wang, C. Ye, K. Huang, M. Motapothula, H. Xing, X. Li, D. C. Qi, X. Li, X. R. Wang, Enhanced metal-insulator transition in freestanding VO_2 down to 5 nm thickness. *ACS Appl. Mater. Interfaces* **13**, 16688–16693 (2021).
19. Y. Chen, Z. Wang, S. Chen, H. Ren, L. Wang, G. Zhang, Y. Lu, J. Jiang, C. Zou, Y. Luo, Non-catalytic hydrogenation of VO_2 in acid solution. *Nat. Commun.* **9**, 818 (2018).
20. W. D. Kaplan, D. Chatain, P. Wynblatt, W. C. Carter, A review of wetting versus adsorption, complexions, and related phenomena: The rosetta stone of wetting. *J. Mater. Sci.* **48**, 5681–5717 (2013).
21. J. Y. Suh, R. Lopez, L. C. Feldman, R. F. Haglund Jr., Semiconductor to metal phase transition in the nucleation and growth of VO_2 nanoparticles and thin films. *J. Appl. Phys.* **96**, 1209–1213 (2004).
22. K. R. Williams, R. S. Muller, Etch rates for micromachining processing. *J. Microelectromech. Syst.* **5**, 256–269 (1996).
23. H. W. Chen, C. I. Li, C. H. Ma, Y. H. Chu, H. L. Liu, Strain engineering of optical properties in transparent VO_2/muscovite heterostructures. *Phys. Chem. Chem. Phys.* **23**, 8908–8915 (2021).
24. C. Cheng, K. Liu, B. Xiang, J. Suh, J. Wu, Ultra-long, free-standing, single-crystalline vanadium dioxide micro/nanowires grown by simple thermal evaporation. *Appl. Phys. Lett.* **100**, 103111 (2012).
25. J. Cao, E. Ertekin, V. Srinivasan, W. Fan, S. Huang, H. Zheng, J. W. Yim, D. R. Khanal, D. F. Ogletree, J. C. Grossman, J. Wu, Strain engineering and one-dimensional organization of metal-insulator domains in single-crystal vanadium dioxide beams. *Nat. Nanotechnol.* **4**, 732–737 (2009).
26. G. Zhou, P. Dai, J. Wu, B. Jin, Q. Wen, G. Zhu, Z. Shen, C. Zhang, L. Kang, W. Xu, J. Chen, P. Wu, Broadband and high modulation-depth THz modulator using low bias controlled VO_2-integrated metasurface. *Opt. Express* **25**, 17322–17328 (2017).
27. M. Seo, J. Kyoung, H. Park, S. Koo, H. S. Kim, H. Bernien, B. J. Kim, J. H. Choe, Y. H. Ahn, H. T. Kim, N. Park, Q. H. Park, K. Ahn, D. S. Kim, Active terahertz nanoantennas based on VO_2 phase transition. *Nano Lett.* **10**, 2064–2068 (2010).
28. H. Cai, S. Chen, C. Zou, Q. Huang, Y. Liu, X. Hu, Z. Fu, Y. Zhao, H. He, Y. Lu, Multifunctional hybrid metasurfaces for dynamic tuning of terahertz waves. *Adv. Opt. Mater.* **6**, 1800257 (2018).
29. F. Hu, Y. Li, X. Xu, Y. Zhou, Y. Chen, P. Zhu, S. Zhao, W. Jiang, W. Zhang, J. Han, Y. Chen, Broadband large-modulation-depth low-current-triggered terahertz intensity modulator based on VO_2 embedded hybrid metamaterials. *Appl. Phys. Express* **11**, 092004 (2018).
30. Y. G. Jeong, H. Bernien, J. S. Kyoung, H. R. Park, H. S. Kim, J. W. Choi, B. J. Kim, H. Kim, K. J. Ahn, D. S. Kim, Electrical control of terahertz nano antennas on VO_2 thin film. *Opt. Express* **19**, 21211–21215 (2011).
31. Z. Sun, A. Martinez, F. Wang, Optical modulators with 2D layered materials. *Nat. Photonics* **10**, 227–238 (2016).
32. C. Han, E. P. J. Parrott, G. Humbert, A. Crunteanu, E. Pickwell-MacPherson, Broadband modulation of terahertz waves through electrically driven hybrid bowtie antenna-VO_2 devices. *Sci. Rep.* **7**, 12725 (2017).
33. F. Fu, L. Shang, Z. Chen, Y. Yu, Y. Zhao, Bioinspired living structural color hydrogels. *Sci. Robot.* **3**, eaar8580 (2018).
34. X. Du, H. Cui, T. Xu, C. Huang, Y. Wang, Q. Zhao, Y. Xu, X. Wu, Reconfiguration, camouflage, and color-shifting for bioinspired adaptive hydrogel-based millirobots. *Adv. Funct. Mater.* **30**, 1909202 (2020).
35. H. Kim, H. Lee, I. Ha, J. Jung, P. Won, H. Cho, J. Yeo, S. Hong, S. Han, J. Kwon, K.-J. Cho, S. H. Ko, Biomimetic color changing anisotropic soft actuators with integrated metal nanowire percolation network transparent heaters for soft robotics. *Adv. Funct. Mater.* **28**, 1801847 (2018).
36. K. Tang, X. Wang, K. Dong, Y. Li, J. Li, B. Sun, X. Zhang, C. Dames, C. Qiu, J. Yao, J. Wu, A thermal radiation modulation platform by emissivity engineering with graded metal-insulator transition. *Adv. Mater.* **32**, 1907071 (2020).
37. K. Tang, K. Dong, C. J. Nicolai, Y. Li, J. Li, S. Lou, C.-W. Qiu, D. H. Raulet, J. Yao, J. Wu, Millikelvin-resolved ambient thermography. *Sci. Adv.* **6**, eabd8688 (2020).
38. M. Marezio, D. B. McWhan, J. P. Remeika, P. D. Dernier, Structural aspects of the metal-insulator transitions in Cr-doped VO_2. *Phys. Rev. B* **5**, 2541–2551 (1972).
39. X. Jin, H. Tan, Z. Wu, J. Liang, W. Miao, C. S. Lian, J. Wang, K. Liu, H. Wei, C. Feng, P. Liu, Y. Wei, Q. Li, J. Wang, L. Liu, X. Li, S. Fan, W. Duan, K. Jiang, Continuous, ultra-lightweight, and multipurpose super-aligned carbon nanotube tapes viable over a wide range of temperatures. *Nano Lett.* **19**, 6756–6764 (2019).
40. D. Lu, D. J. Baek, S. S. Hong, L. F. Kourkoutis, Y. Hikita, H. Y. Hwang, Synthesis of freestanding single-crystal perovskite films and heterostructures by etching of sacrificial water-soluble layers. *Nat. Mater.* **15**, 1255–1260 (2016).
41. Y. Zhang, L. Shen, M. Liu, X. Li, X. Lu, L. Lu, C. Ma, C. You, A. Chen, C. Huang, L. Chen, M. Alexe, C. L. Jia, Flexible quasi-two-dimensional $CoFe_2O_4$ epitaxial thin films for continuous strain tuning of magnetic properties. *ACS Nano* **11**, 8002–8009 (2017).

42. J. Qiao, S. Wang, Z. Wang, C. He, S. Zhao, X. Xiong, S. Wang, X. Zhang, X. Tao, Ultrasensitive and broadband all-optically controlled THz modulator based on $MoTe_2$/Si van der Waals heterostructure. *Adv. Opt. Mater.* **8**, 2000160 (2020).
43. Z. W. Shi, X. X. Cao, Q. Y. Wen, T. L. Wen, Q. H. Yang, Z. Chen, W. S. Shi, H. W. Zhang, Terahertz modulators based on silicon nanotip array. *Adv. Opt. Mater.* **6**, 1700620 (2018).
44. W. L. Chan, H. T. Chen, A. J. Taylor, I. Brener, M. J. Cich, D. M. Mittleman, A spatial light modulator for terahertz beams. *Appl. Phys. Lett.* **94**, 213511 (2009).
45. H. Ma, Y. Wang, R. Lu, F. Tan, Y. Fu, G. Wang, D. Wang, K. Liu, S. Fan, K. Jiang, X. Zhang, A flexible, multifunctional, active terahertz modulator with an ultra-low triggering threshold. *J. Mater. Chem. C* **8**, 10213–10220 (2020).
46. B. Sensale-Rodriguez, R. Yan, S. Rafique, M. Zhu, W. Li, X. Liang, D. Gundlach, V. Protasenko, M. M. Kelly, D. Jena, L. Liu, H. G. Xing, Extraordinary control of terahertz beam reflectance in graphene electro-absorption modulators. *Nano Lett.* **12**, 4518–4522 (2012).
47. S. Chen, F. Fan, Y. Miao, X. He, K. Zhang, S. Chang, Ultrasensitive terahertz modulation by silicon-grown MoS_2 nanosheets. *Nanoscale* **8**, 4713–4719 (2016).
48. H. T. Chen, W. J. Padilla, J. M. Zide, A. C. Gossard, A. J. Taylor, R. D. Averitt, Active terahertz metamaterial devices. *Nature* **444**, 597–600 (2006).
49. H.-T. Chen, W. J. Padilla, M. J. Cich, A. K. Azad, R. D. Averitt, A. J. Taylor, A metamaterial solid-state terahertz phase modulator. *Nat. Photonics* **3**, 148–151 (2009).
50. J. Kyoung, M. Seo, H. Park, S. Koo, H. S. Kim, Y. Park, B. J. Kim, K. Ahn, N. Park, H. T. Kim, D. S. Kim, Giant nonlinear response of terahertz nanoresonators on VO_2 thin film. *Opt. Express* **18**, 16452–16459 (2010).
51. Z. Fan, Z. Geng, X. Lv, Y. Su, Y. Yang, J. Liu, H. Chen, Optical controlled terahertz modulator based on tungsten disulfide nanosheet. *Sci. Rep.* **7**, 14828 (2017).
52. H. Kim, Y. Kim, K. S. Kim, H. Y. Jeong, A.-R. Jang, S. H. Han, D. H. Yoon, K. S. Suh, H. S. Shin, T. Y. Kim, W. S. Yang, Flexible thermochromic window based on hybridized VO_2/graphene. *ACS Nano* **7**, 5769–5776 (2013).
53. S. Bhupathi, S. Wang, M. Abutoama, I. Balin, L. Wang, P. G. Kazansky, Y. Long, I. Abdulhalim, Femtosecond laser-induced vanadium oxide metamaterial nanostructures and the study of optical response by experiments and numerical simulations. *ACS Appl. Mater. Interfaces* **12**, 41905–41918 (2020).
54. C. I. Li, J. C. Lin, H. J. Liu, M. W. Chu, H. W. Chen, C. H. Ma, C. Y. Tsai, H. W. Huang, H. J. Lin, H. L. Liu, P. W. Chiu, Y. H. Chu, Van der Waal epitaxy of flexible and transparent VO_2 film on muscovite. *Chem. Mater.* **28**, 3914–3919 (2016).
55. Y. Chen, L. Fan, Q. Fang, W. Xu, S. Chen, G. Zan, H. Ren, L. Song, C. Zou, Free-standing SWNTs/VO_2/Mica hierarchical films for high-performance thermochromic devices. *Nano Energy* **31**, 144–151 (2017).
56. T. Chang, Y. Zhu, J. Huang, H. Luo, P. Jin, X. Cao, Flexible VO_2 thermochromic films with narrow hysteresis loops. *Sol. Energ. Mat. Sol. C.* **219**, 110799 (2021).
57. H. Zong, H. Liu, L. Yan, Y. Yin, L. Bian, C. Kang, G. Cao, M. Li, Synchronized improvements of luminous transmittance and solar modulation ability of VO_2 films by employing SnO_2 buffer layers. *Thin Solid Films* **709**, 138174 (2020).
58. P. Zhang, W. Zhang, J. Wang, K. Jiang, J. Zhang, W. Li, J. Wu, Z. Hu, J. Chu, The electro-optic mechanism and infrared switching dynamic of the hybrid multilayer VO_2/Al:ZnO heterojunctions. *Sci. Rep.* **7**, 4425 (2017).
59. T. Kang, Z. Ma, J. Qin, Z. Peng, W. Yang, T. Huang, S. Xian, S. Xia, W. Yan, Y. Yang, Z. Sheng, J. Shen, C. Li, L. Deng, L. Bi, Large-scale, power-efficient Au/VO_2 active metasurfaces for ultrafast optical modulation. *Nanophotonics* **10**, 909–918 (2021).
60. G. Sun, X. Cao, X. Gao, S. Long, M. Liang, P. Jin, Structure and enhanced thermochromic performance of low-temperature fabricated VO_2/V_2O_3 thin film. *Appl. Phys. Lett.* **109**, 143903 (2016).
61. Z. Tian, B. Xu, B. Hsu, L. Stan, Z. Yang, Y. Mei, Reconfigurable vanadium dioxide nanomembranes and microtubes with controllable phase transition temperatures. *Nano Lett.* **18**, 3017–3023 (2018).
62. J. S. Sim, Y. Zhou, S. Ramanathan, Suspended sub-50 nm vanadium dioxide membrane transistors: fabrication and ionic liquid gating studies. *Nanoscale* **4**, 7056–7062 (2012).
63. Q. Shi, W. Huang, Y. Zhang, J. Yan, Y. Zhang, M. Mao, Y. Zhang, M. Tu, Giant phase transition properties at terahertz range in VO_2 films deposited by sol-gel method. *ACS Appl. Mater. Interfaces* **3**, 3523–3527 (2011).
64. H.-F. Zhu, L.-H. Du, J. Li, Q.-W. Shi, B. Peng, Z.-R. Li, W.-X. Huang, L.-G. Zhu, Near-perfect terahertz wave amplitude modulation enabled by impedance matching in VO_2 thin films. *Appl. Phys. Lett.* **112**, 081103 (2018).
65. S. Chen, H. Yuan, Z. Zhai, L. Du, S. Zhong, H. Zhu, Q. Shi, W. Huang, Z. Li, L. Zhu, All optically driven memory device for terahertz waves. *Opt. Lett.* **45**, 236–239 (2020).
66. X. Wu, Z. Wu, C. Ji, H. Zhang, Y. Su, Z. Huang, J. Gou, X. Wei, J. Wang, Y. Jiang, THz transmittance and electrical properties tuning across IMT in vanadium dioxide films by Al doping. *ACS Appl. Mater. Interfaces* **8**, 11842–11850 (2016).
67. C. Ji, Z. Wu, X. Wu, H. Feng, J. Wang, Z. Huang, H. Zhou, W. Yao, J. Gou, Y. Jiang, Optimization of metal-to-insulator phase transition properties in polycrystalline VO_2 films for terahertz modulation applications by doping. *J. Mater. Chem. C* **6**, 1722–1730 (2018).
68. H. Zhang, Z. Wu, R. Niu, X. Wu, Q. He, Y. Jiang, Metal–insulator transition properties of sputtered silicon-doped and un-doped vanadium dioxide films at terahertz range. *Appl. Surf. Sci.* **331**, 92–97 (2015).
69. A. Pashkin, C. Kübler, H. Ehrke, R. Lopez, A. Halabica, R. F. Haglund, R. Huber, A. Leitenstorfer, Ultrafast insulator-metal phase transition in VO_2 studied by multiterahertz spectroscopy. *Phys. Rev. B* **83**, 195120 (2011).
70. D. Fu, K. Liu, T. Tao, K. Lo, C. Cheng, B. Liu, R. Zhang, H. A. Bechtel, J. Wu, Comprehensive study of the metal-insulator transition in pulsed laser deposited epitaxial VO_2 thin films. *J. Appl. Phys.* **113**, 043707 (2013).
71. Z. Ren, L. Cheng, L. Hu, C. Liu, C. Jiang, S. Yang, Z. Ma, C. Zhou, H. Wang, X. Zhu, Y. Sun, Z. Sheng, Photoinduced broad-band tunable terahertz absorber based on a VO_2 thin film. *ACS Appl. Mater. Interfaces* **12**, 48811–48819 (2020).
72. W. Liang, Y. Jiang, J. Guo, N. Li, W. Qiu, H. Yang, Y. Ji, S. N. Luo, Van der Waals heteroepitaxial VO_2/Mica films with extremely low optical trigger threshold and large THz field modulation depth. *Adv. Opt. Mater.* **7**, 1900647 (2019).
73. C. Chen, Y. Zhu, Y. Zhao, J. H. Lee, H. Wang, A. Bernussi, M. Holtz, Z. Fan, VO_2 multidomain heteroepitaxial growth and terahertz transmission modulation. *Appl. Phys. Lett.* **97**, 211905 (2010).

Acknowledgments

Funding: This work was financially supported by the Basic Science Center Project of NSFC under grant no. 51788104, the National Key R&D Program of China (2018YFA0208401), the National Natural Science Foundation of China (grant nos. 51802008, 12074020, and 61735002), the Beijing Nova Program (no. Z20110006820111), the Beijing Natural Science Foundation (grant no. Z180015), the General Project of Beijing Municipal Education Commission (grant no. KM201910005014), and the State Key Laboratory of New Ceramic and Fine Processing Tsinghua University (KF202003). **Author contributions:** X.Z., H.M., and K.L. conceived the project. H.M., Y.W., and X.X. prepared the f-VO_2 film and performed characterizations. Y.S., E.W., and B.W. measured the surface morphology of the f-VO_2 film. X.G., H.M., and K.J. measured the mechanical property of the f-VO_2 film. H.M. and X.X. prepared thermochromism actuators and measure their performance in the actuation and the thermochromism. H.M. prepared the temperature-measuring strip based on the f-VO_2/PI film and measure their performance. H.M. and Y.W. prepared the f-VO_2/CNT film and measure their performance in the THz modulation. H.M., K.L., and X.Z. wrote the manuscript. All authors participated in discussing the results. **Competing interests:** The authors declare that they have no competing interests. **Data and materials availability:** All data needed to evaluate the conclusions in the paper are present in the paper and/or the Supplementary Materials.

Submitted 9 July 2021
Accepted 18 October 2021
Published 8 December 2021
10.1126/sciadv.abk3438